

# Origin of piezoelectric response under a biased scanning probe microscopy tip across a 180° ferroelectric domain wall

Shiming Lei,<sup>1,2</sup> Eugene A. Eliseev,<sup>3</sup> Anna N. Morozovska,<sup>4</sup> Ryan C. Haislmaier,<sup>2</sup> Tom T. A. Lummen,<sup>2</sup> W. Cao,<sup>1,5,\*</sup> Sergei V. Kalinin,<sup>6</sup> and Venkatraman Gopalan<sup>2,†</sup>

<sup>1</sup>*Condensed Matter Science and Technology Institute and Department of Physics, Harbin Institute of Technology, Harbin 150080, People's Republic of China*

<sup>2</sup>*Materials Research Institute and Department of Materials Science and Engineering, Pennsylvania State University, 212-N MSC Building, University Park, Pennsylvania 16802, USA*

<sup>3</sup>*Institute for Problems of Materials Science, National Academy of Science of Ukraine, 3, Krjijanovskogo, 03142 Kiev, Ukraine*

<sup>4</sup>*Institute of Physics, National Academy of Sciences of Ukraine, 46, Nauki, 03028 Kiev, Ukraine*

<sup>5</sup>*Materials Research Institute and Department of Mathematics, Pennsylvania State University, University Park, Pennsylvania 16802, USA*

<sup>6</sup>*The Center for Nanophase Materials Sciences, Oak Ridge National Laboratory, Oak Ridge, Tennessee 37831, USA*

(Received 26 May 2012; published 22 October 2012)

The piezoelectric response of a material under a nanoscale biased tip scanned across a sample in piezoelectric force microscopy (PFM) provides insight into the structure and dynamics of domain walls in ferroelectrics. While the vertical displacements of the tip under piezoelectric deformations of the sample have been reasonably explained, the origin of the lateral twisting of the tip remains unclear. This poses a serious problem when combining vertical and lateral signals to create vector PFM maps of polarization distribution in ferroelectrics. Using a combination of finite element modeling and analytical theory, and by comparison with prior experimental work across a single antiparallel domain wall on the (0001) surface of LiNbO<sub>3</sub>, we unequivocally show that the lateral signal originates from a shear displacement of the surface. We show that there are two types of lateral signals, one arising from the  $d_{15}$  shear deformation, and the other from the  $d_{22}$  lateral deformation. The vertical PFM signal surprisingly shows equal contributions from the  $d_{33}$  (leading to normal displacements) and  $d_{15}$  (leading to shear displacement) coefficients. We also show that an averaging of the PFM signal over a finite contact area of the tip, as experimentally observed, is essential to understanding the line shape of the PFM responses across the wall. After clarifying the origin of the nanoscale PFM signals, we conclude that, in general, a vertical signal does *not* automatically indicate a polarization component out of the surface, while a lateral signal does *not* automatically indicate an in-plane polarization component. Without a detailed theory or simulation especially in materials with nanoscale domain structures, ferroelectric relaxors, and morphotropic compositions, such assumptions may lead to incorrect domain and wall interpretations. The proposed model and numerical simulation method could be applied to all piezoelectric materials.

DOI: [10.1103/PhysRevB.86.134115](https://doi.org/10.1103/PhysRevB.86.134115)

PACS number(s): 77.80.Fm, 77.65.-j, 77.22.Ej

## I. INTRODUCTION

The defining feature of ferroelectric materials is a built-in spontaneous electrical polarization that is switchable with an electric field. Ferroelectric domains, the regions of uniform ferroelectric polarization separated by domain walls, influence all macroscopic properties of ferroelectrics. While electrical and optical techniques have been widely used to probe ferroelectric domains and domain walls, more recently, piezoelectric force microscopy (PFM) has emerged as a tool of choice for probing and imaging domain structures in conventional<sup>1–13</sup> and relaxor ferroelectrics.<sup>14–17</sup> Converse piezoelectric effect induces a strain in the material under an electric field. Using a nanoscale electrically biased tip in contact with the surface of a ferroelectric material, the resultant piezoelectric displacements of the surface are then transduced in the form of tip displacements in PFM that are detected optically. The piezoelectric tensor,  $d_{ijk}$ , is nonzero only in the absence of inversion symmetry. Therefore, all ferroelectrics exhibit piezoelectric response, where  $d_{ijk}$  is linearly proportional to the spontaneous polarization  $P_s$ . Beyond imaging, single point hysteresis loop measurements by PFM<sup>6,9,18–25</sup> and spectroscopic hysteresis loop imaging<sup>26,27</sup> allowed local probing of polarization dynamics in nanoscale,

as discussed in detail in many reviews.<sup>10,28–30</sup> The capability for probing<sup>31,32</sup> and manipulating<sup>4,33</sup> the local polarization reversal on a single defect level has also been demonstrated.

Quantitative theoretical and simulation methods have become increasingly important in order to correctly interpret the PFM images and to understand the fundamental image formation mechanisms involved towards extracting the fundamental physical properties of domain walls. The universal approach for the calculation of electromechanical response in PFM based on decoupled theory by Felten *et al.*<sup>12</sup> and Scrymgeour and Gopalan<sup>13</sup> has been developed. Using decoupled theory for PFM response of semi-infinite materials, Refs. 34 and 35 obtained analytical expressions for *vertical* PFM resolution function and domain-wall profiles, and developed the theoretical framework for interpretation of PFM spectroscopy data,<sup>36–38</sup> which was an important step towards understanding the origin of lateral PFM. Vertical PFM signal refers to the displacement of the tip perpendicular to the sample surface undergoing a piezoelectric displacement.

In comparison to the vertical PFM, the *lateral* PFM is not completely understood both theoretically and experimentally.<sup>39–42</sup> Lateral PFM refers to the lateral or sideways twisting of the PFM tip due to the sample piezoelectric

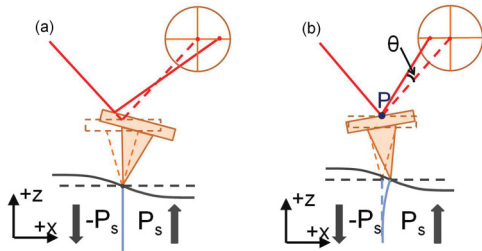


FIG. 1. (Color online) Comparison of the two mechanisms explaining the  $0^\circ$  lateral PFM: (a) slope model; (b) effective shear model. In (b), the pivot point is labeled as P, and twisting angle of the cantilever as  $\theta$ .

displacements. Note that a combination of vertical and lateral PFM signals are often used in order to create what is referred to as *vector* PFM plots,<sup>43</sup> which are then used to interpret the direction of ferroelectric polarizations in different domains. However, a serious limitation in this approach arises from the assumption that the lateral PFM signal originates from ferroelectric polarization components in the plane of the sample surface, and vertical PFM originates from out-of-plane polarization components, as is often done.<sup>44–46</sup> As we show in this paper, such a simple qualitative interpretation of PFM signals is violated in the vicinity of ferroelectric domain walls, and can lead to incorrect domain structure interpretations.

Scrymgeour and Gopalan suggested a slope model,<sup>13</sup> where topological changes to the sample surface result in twisting of the tip under a vertical force pressed against a slanted sample surface (see Fig. 1). Jungk and Soergel argued against the slope model and instead proposed a model based on local electric field arising from the surface polarization charge near domain walls,<sup>42</sup> but later ruled out this claim.<sup>41</sup> Paruch and co-workers<sup>39,40</sup> experimentally confirmed the initial shear model proposed in Ref. 36, and presented a preliminary intuitive vertical expansion/contraction mechanism through the sign change of the  $d_{33}$  piezoelectric coefficient across an antiparallel domain wall. Soergel *et al.*<sup>41</sup> observed a lateral signal at the domain boundaries of  $\text{LiNbO}_3$ ,  $\text{BaTiO}_3$ , and  $\text{KTiOPO}_4$  single crystals and attempted to quantitatively compare their results to the existing models, but concluded that both the slope and the shear from expansion/contraction models were inadequate. Thus, to date, there is no general agreement on the origin of lateral PFM response at the domain walls. This motivates us to perform a thorough theoretical and experimental study of lateral PFM signal. Using the finite element method (FEM) combined with analytical theory and experimental measurements, we have performed a detailed study of lateral PFM across a single  $180^\circ$  domain wall in  $\text{LiNbO}_3$ . Our study resolves the major issues surrounding the interpretation of lateral piezoelectric response at such a  $180^\circ$  ferroelectric domain wall by showing that a shear model [Fig. 1(b)] is correct. However, the origin of the sample shear is more complex than assumed before and is dominated by the piezoelectric coefficient  $d_{15}$ , instead of those proposed in the past expansion/contraction models ( $d_{33}$  and  $d_{31}$ ).<sup>39–41</sup> The work also predicts two types of lateral signals (which are later labeled as  $0^\circ$  and  $90^\circ$  lateral PFM signals); the only experiments<sup>13</sup> to show this latter signal were dismissed as an

artefact. In addition to FEM simulation, a revised analytical theory is now presented which predicts this signal. We also propose an averaging method for all the PFM signals over a finite contact area of the tip on the sample surface, which resolves the line-shape arguments raised by Soergel<sup>41</sup> and leads to the best agreement of the PFM line shapes across domain walls between theory, simulation, and experiments.

The organization of the paper is as follows: We discuss the FEM simulation method of the PFM process in the decoupled approximation framework in Sec. II, followed by comparing the experimental data, FEM modeling, and analytical theory in Secs. III and IV. Finally, discussion and conclusions are given in Secs. V and VI, respectively.

## II. FINITE ELEMENT ANALYSIS

Finite element method (FEM) was utilized to model PFM using the commercial software ANSYS<sup>TM</sup>. A complete description of the FEM modeling of the PFM can be found in Ref. 13. The current work simulates tip shape and field distribution more precisely by using the finite element method, while Ref. 13 uses an analytical model for calculating the field distribution. In addition, the current work assumes true tip-sample contact while Ref. 13 assumes a noncontact geometry with a dielectric gap. An actual PFM experiment is performed using an ac voltage with a frequency of  $f < 100$  kHz applied to the tip, which is scanned at a rate of  $\sim 0.1$   $\mu\text{m/s}$  in contact with the sample surface. In contrast, the FEM simulations are quasistatic in that the applied voltage is dc, and the tip position during the simulation is fixed relative to the sample surface and the domain wall. The simulation also assumes a *decoupled approximation* framework,<sup>12,13,36</sup> where the potential distribution in the sample due to the biased tip is first calculated, followed by the calculation of the piezoelectric displacements in response to this potential. A set of full piezoelectric, dielectric, and elastic tensors for  $\text{LiNbO}_3$  (Ref. 47) were used as the input parameters, thus providing a rigorous three-dimensional (3D) analysis.

In our simulation, a thin  $180^\circ$  domain wall was created in the  $y$ - $z$  plane of the model coordinate system (see Fig. 1), and it corresponds to one of the three degenerate  $\{11\bar{2}0\}$  planes in  $\text{LiNbO}_3$ . For the  $x > 0$  domain, the polarization direction is in the  $+z$  direction; for the  $x < 0$  domain, the polarization direction is in the  $-z$  direction. In order to simulate the PFM scan operation on the sample, a series of simulations have been carried out with the tip at different positions on the sample surface across the domain wall. Our simulations were performed with the same  $180^\circ$  steplike domain wall. A comparison between the FEM results and experiment data indicates that the effect of intrinsic diffusive domain wall is so small that it does not have any significant contribution to the PFM signal.

The tip model used in our simulation is disk type, the same as the one used in Ref. 38. It has a cone-shaped geometry with a circular disk-type end, which is in true contact with the sample surface (Fig. 2). This geometry was confirmed by scanning electron microscopy after experimental scans.<sup>38,41</sup> In order to make a realistic comparison with experiments, the radius of the circular tip-surface contact area is set as  $r = 50$  nm for the vertical PFM simulation and  $r = 55$  nm for the

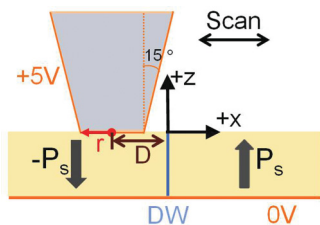


FIG. 2. (Color online) Schematic of the PFM measurement across 180° domain wall in FEM simulation. The polarization for the right domain points up, while the left domain points down.  $r$  is the radius of the circular tip-sample contact area.  $D$  is the distance between tip center and domain wall.

0° lateral PFM simulation, consistent with experimental PFM scans in Ref. 48. For all simulations, the tip has a length of 10 μm with a full cone angle of 30°. A constant electric voltage +5 V is applied to the tip surface and the bottom surface of the sample is set as 0 V. The sample in our simulation is a block with the size of 8 × 8 × 1 μm. In this work, the potential distribution in the sample was first calculated, followed by the calculation of the piezoelectric displacements in response to this potential. The bottom surface displacements of the sample,  $U_x$ ,  $U_y$ , and  $U_z$  are confined to 0, corresponding to a clamped bottom surface. The meshing was adjusted fine enough to yield results independent of the meshing size.

The mechanical boundary conditions at the ferroelectric surface below the tip are an important consideration in FEM modeling. In both FEM and decoupled approximation, we consider the surface as mechanically free and calculate the

local PFM response defined as the surface displacement in the central point ( $r = 0$ ) just below the tip. The limiting case corresponds to the absence of indentation (hypothetical case of the weightless and frictionless cantilever) and is consistent with all previous theoretical studies.<sup>12,13,34–38</sup> The local PFM response calculated for the mechanically free conditions provides the first-order approximation for PFM signal in general. FEM results for both vertical and lateral PFM surface displacements were averaged over the contact area (radius of the squashed tip,  $r = a$ ) using the following equation:

$$U_i(D) = \frac{1}{\pi a^2} \int_0^a \int_0^{2\pi} r u_i(r, \varphi, D) dr d\varphi (i = x, y, z). \quad (1)$$

A derivation of Eq. (1), based on force arguments, is given in Appendix A. The key assumptions in the averaging model are that the tip-sample interface is *intimate* and *conformal*, i.e., there is no relative motion of the tip with respect to the sample surface, and they remain in intimate contact even after piezoelectric deformation. A pivot point is defined at the top center of the conical tip (Fig. 1), where the cantilever arm joins the cone from where the tip displacement is read using optical means. The displacements of this pivot point are not constrained in the  $z$  direction ( $U_{z,pivot} \neq 0$ ) which allows for the vertical PFM signal detection, but the lateral displacements of this pivot are clamped by the cantilever arm ( $U_{x,pivot}, U_{y,pivot} = 0$ ) which only allows twisting of the conical part of the tip. If the conical tip/sample surface interface displaces in the lateral direction, it will give rise to lateral PFM signal. Note that the PFM signal naturally averages

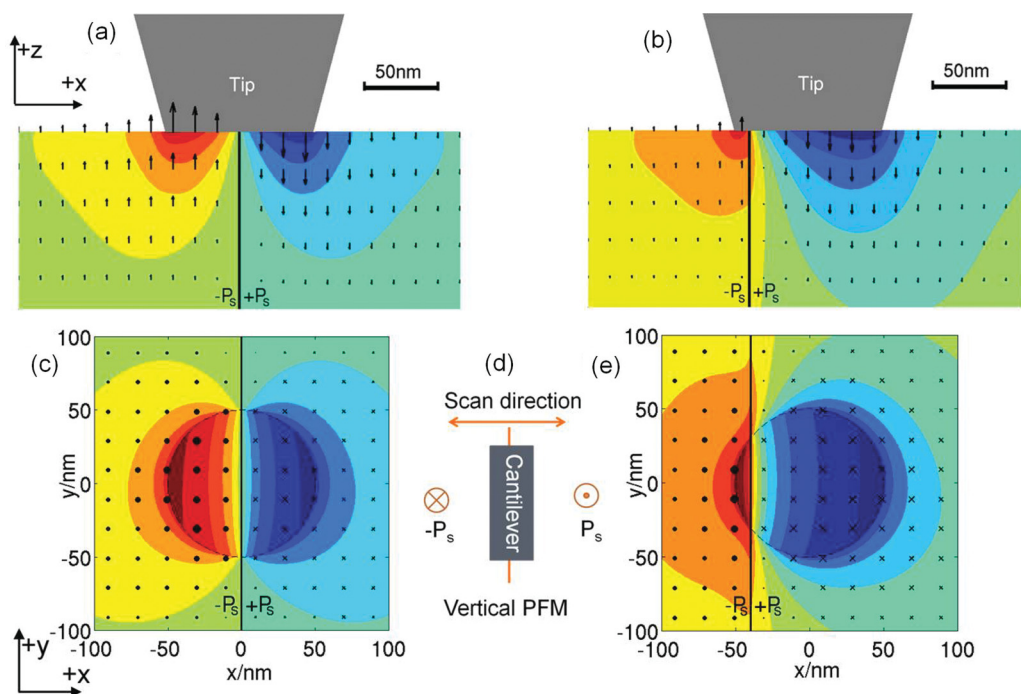


FIG. 3. (Color online) Cross-section view (a), (b) and top view (c), (e) for the quiver plot of the vertical displacement of the sample in the vertical PFM simulation. The tip-domain wall distance,  $D = 0$  for (a), (c) and  $D = 40$  nm for (b), (e). The radius of the circular tip-surface contact area  $r = 50$  nm. (d) Schematic of cantilever direction with respect to the domain wall for the vertical PFM scan. The electric voltage applied on the tip is +5 V. The sample generated a positive vertical displacement for the left domain and a negative vertical displacement for the right domain.

in going from the displacement field at the tip sample interface to a single pivot point on the top.

### III. VERTICAL PFM RESPONSE: SIMULATIONS, THEORY, AND EXPERIMENTS

The vertical PFM signal originates from an out-of-plane displacement of the sample surface,  $U_z$ .<sup>28,30,43,49,50</sup> Shown in Fig. 3 is a cross-sectional and top-down view of a quiver plot and contour plot of the  $z$ -component displacement of the sample. Unlike Ref. 13 where only surface displacements are shown, both surface and depth displacement fields are shown here. For the tip lying in the middle of the domain wall,  $D = 0$ , and for the tip lying 40 nm away from the domain wall,  $D = 40$  nm.

The vertical PFM simulation yielded expected results: the left and right domain in Fig. 3 undergo positive and negative  $z$ -component displacements, respectively. The sample surface displacement underneath the tip has a nonuniform distribution. Here we compare two interpretations of the vertical PFM signal: (1) use the displacement of the center point in the circular contact area to represent the tip displacement; (2) integrate the displacement over the circular contact area to give the displacement value of the tip according to Eq. (1). After such analysis for each simulation with the tip lying in different positions away from the domain wall, the results are given in Fig. 4.

Also shown in Fig. 4 is experimental data<sup>48</sup> with results from analytical theory.<sup>36,37</sup> Note that Fig. 4 also includes relative phase information based on the data from Ref. 48. One can see from Fig. 4 that the FEM area integration averaging method results have the best agreement with experimental data, while the FEM center result matches well with the analytical theory. When the tip lies 400 nm away from the

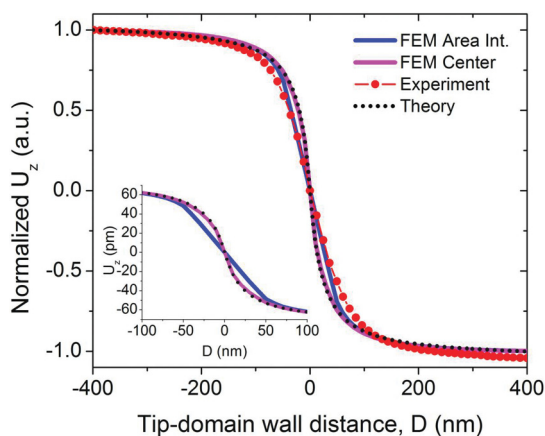


FIG. 4. (Color online) Comparison of the normalized vertical PFM signal ( $U_z$ ) from the FEM results, experiment, and analytical theory. FEM Area Int. indicates the curve is obtained from integration of the  $z$ -component displacement over circular tip-sample contact area as Eq. (1). In comparison, “FEM Center” indicates that the curve is from the exact center point of the tip-sample contact region. The experiment data is from Ref. 48. “Theory” indicates the result of analytical theory (Refs. 36 and 37). Inset shows the non-normalized displacement value from the FEM results and analytical theory. The Poisson’s ratio is set as  $\nu = 0.35$  for the analytical theory.

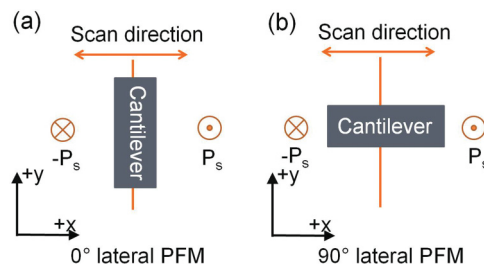


FIG. 5. (Color online) Schematic of (a)  $0^\circ$  lateral PFM scan and (b)  $90^\circ$  lateral PFM scan.

domain wall, both averaging methods from FEM give 70.0 pm for the  $z$ -component displacement, as compared to 70.9 pm from analytical theory, with a tip bias of +5 V. In order to test how the tip displacement saturates as it moves away from the domain wall, an additional simulation for the tip lying far away from the domain wall was performed. The single domain calculation gives the  $z$ -component displacement 70.1 pm, which suggests that the vertical PFM signal for the tip lying 400 nm away from the domain wall already reaches more than 99% of the saturation value.

From the vertical PFM simulation, one can see that the FEM model used here with area integration treatment [Eq. (1)] shows excellent quantitative agreement with the experiment. This provides us confidence in the following lateral PFM simulations.

### IV. LATERAL PFM

In addition to vertical PFM response, two lateral PFM setups are essential to comprehensively determine the domain structure. As is shown in Fig. 5, when the cantilever arm is parallel to the domain wall, we name it  $0^\circ$  lateral PFM (corresponding to  $y$ -LPFM in Ref. 50). When the cantilever is perpendicular to the domain wall, we name it  $90^\circ$  lateral PFM (corresponding to  $x$ -LPFM in Ref. 50). Our FEM simulation results support the interpretation that both types of lateral PFM signals come from the lateral displacement of the sample surface.<sup>36</sup> The  $x$ -component displacement of the sample surface underneath the tip leads to the torsion of the cantilever in the  $x$ - $z$  plane, leading to the  $0^\circ$  lateral PFM signal while the  $y$ -component displacement of the sample surface underneath the tip leads to the torsion of the cantilever in the  $y$ - $z$  plane and accordingly gives rise to the  $90^\circ$  lateral PFM signal. Each of these is described in detail below.

#### A. $0^\circ$ lateral PFM

For the  $0^\circ$  lateral PFM, the  $x$ -component displacement of the sample surface underneath the tip,  $U_x$ , gives the PFM signal. Thus only the data of  $x$ -component displacement of the sample is analyzed. Shown in Fig. 6 are the cross section and top view of the quiver plot and the contour plot of the  $x$ -component displacement of the sample, with  $D = 0$ , and  $D = 40$  nm.

Figure 6 clearly shows that the entire sample surface has a lateral displacement along the  $x$  direction. This leads to a torsion of the PFM cantilever in the  $x$ - $z$  plane for a  $0^\circ$

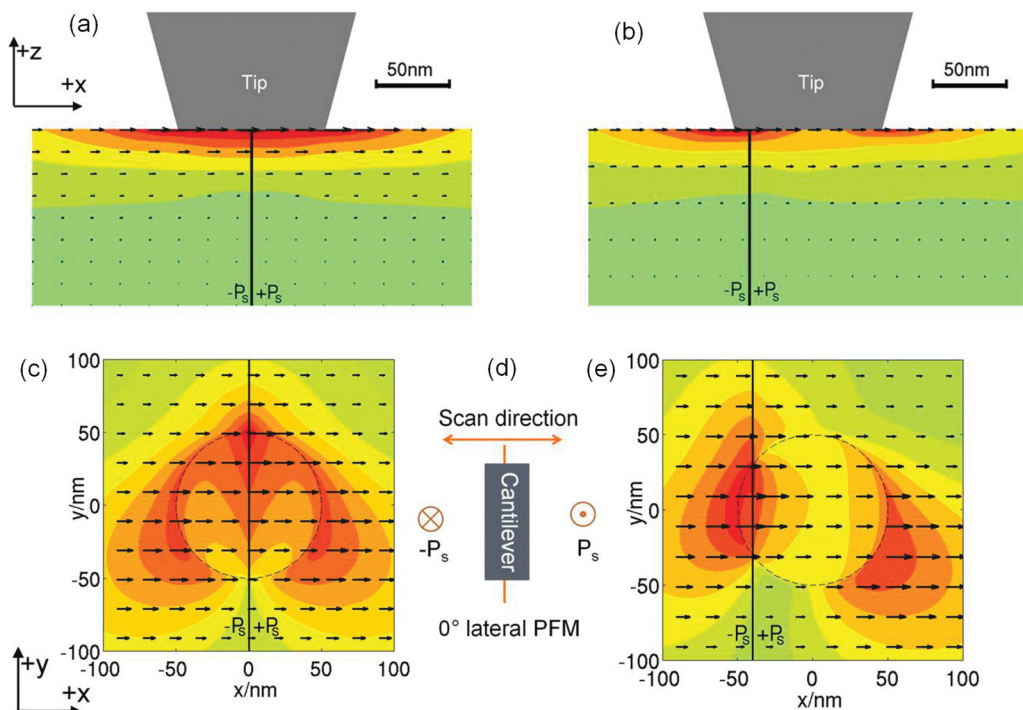


FIG. 6. (Color online) Cross-section view (a), (b) and top view (c), (e) for the quiver plot of the  $x$ -component displacement of the sample in the  $0^\circ$  lateral PFM simulation. The tip-domain wall distance,  $D = 0$  for (a), (c) and  $D = 40$  nm for (b), (e). The radius of the circular tip-surface contact area  $r = 55$  nm. (d) Schematic of cantilever direction with respect to the domain wall for the  $0^\circ$  lateral scan. The electric voltage applied on the tip is  $+5$  V.

lateral PFM scan. A quantitative comparison of the  $0^\circ$  lateral scan result from the FEM slope model,<sup>48</sup> experiment,<sup>48</sup> and analytical theory<sup>36,37</sup> are shown in Fig. 7. For the convenience of comparison,  $\omega_{\text{PFM}}$ , defined as the half width at half maximum (HWHM), is the half width where the PFM signal decreased to half of its peak amplitude. Although the curves in Fig. 7 are similar (with a peak shown when the tip position lies in the middle of the domain wall), the effective shear

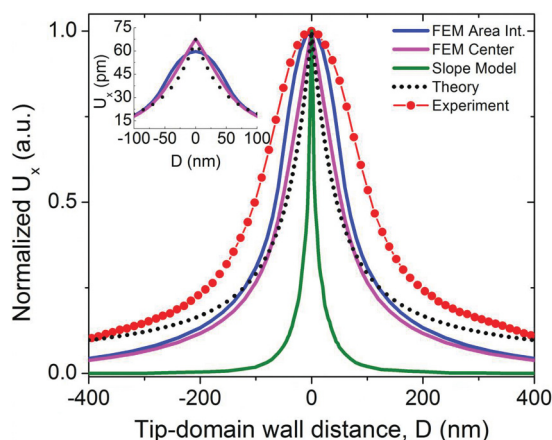


FIG. 7. (Color online) Comparison of the normalized  $0^\circ$  lateral signal from FEM effective shear model, FEM slope model, experiment, and analytical theory. The legend is the same as Fig. 4, except for the slope model. The experiment data and slope model are extracted from Ref. 48. Inset shows the non-normalized value from the FEM results and analytical theory.

model from FEM calculation predicts  $\omega_{\text{PFM}}$  to be 65 nm (area integration method) and 54 nm (center point). In comparison,  $\omega_{\text{PFM}}$  is 102 nm (experiments), 47 nm (analytical theory), and 8 nm (FEM slope model). Note that the area integration method has the best agreement with the experiments, not only in terms of HWHM, but also the shape of the curve near the peak, which shows a continuous slope for the experiments and the area integration method, but has a discontinuous slope for the other approaches shown.

There are still some discrepancies in  $\omega_{\text{PFM}}$  between the experiments and FEM theory using the area integration method, which are likely to involve other aspects of surface physics and contact dynamics that are not fully captured here. For example, it has been shown that the position of the domain wall near the surface is influenced by the high fields under the biased tip leading to a bending of the wall towards or away from the wall,<sup>51</sup> and this could lead to a significant broadening of the lateral PFM signal as large as  $\sim 10$  nm.

**B.  $90^\circ$  lateral PFM**

The  $90^\circ$  lateral PFM signal reflects the  $y$ -component displacement  $U_y$  of the sample surface underneath the tip. Figure 8 displays the cross section and top view of the quiver plot and the contour plot of the  $y$ -component displacement of the sample, with  $D = 0$ , and  $D = 40$  nm.

As shown in Fig. 8, this displacement is qualitatively different from the vertical PFM and the  $0^\circ$  lateral PFM simulations. The scan results are shown in Fig. 9.

Although the earlier version of the analytical theory<sup>36</sup> predicted the correct qualitative vertical and  $0^\circ$  lateral PFM

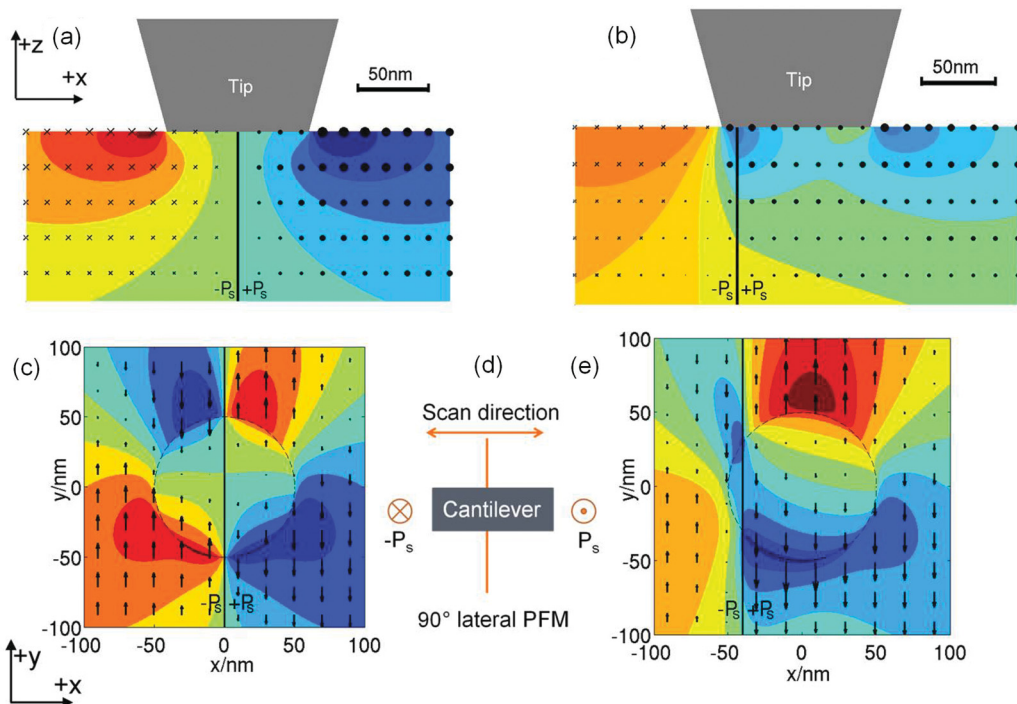


FIG. 8. (Color online) Cross-section view (a), (b) and top view (c), (e) for the quiver plot of the  $y$ -component displacement of the sample in the  $90^\circ$  lateral PFM simulation. The tip-domain wall distance  $D = 0$  for (a), (c) and  $D = 40$  nm for (b), (e). The radius of the circular tip-surface contact area  $r = 50$  nm. (d) Schematic of cantilever direction with respect to the domain wall for the  $90^\circ$  lateral scan. The electric voltage applied on the tip is  $+5$  V.

signals as experiment, it did not predict the  $90^\circ$  lateral PFM signal shown in Fig. 17 of Ref. 13. The reason is that among all the piezoelectric constants,  $d_{22}$  is the dominant piezoelectric constant giving rise to a  $90^\circ$  lateral PFM signal. The earlier version of analytical theory neglected the piezoelectric response from  $d_{22}$ . A revised analytical theory accounting for the  $d_{22}$

coefficient is presented here (see Appendix B), and it indeed predicts a  $90^\circ$  lateral PFM signal qualitatively similar to the FEM calculation, as shown in Fig. 9. The amplitude of the FEM and analytical theory displacements in Fig. 9 (see inset) also qualitatively match with the  $90^\circ$  lateral PFM experiment data reported by Scrymgeour and Gopalan.<sup>13</sup> The experimental  $90^\circ$  lateral PFM signal was reported to be  $\sim 1/10$ th the  $0^\circ$  lateral PFM signal,<sup>13</sup> while the FEM results indicate  $\sim 1/5$ th of the  $0^\circ$  lateral PFM signal; thus it is easy to get cross talk from the  $0^\circ$  lateral PFM signal. The paper reports that even for a rotation of  $\sim 10^\circ$  away from the perpendicular position, the  $90^\circ$  lateral signal resembles the  $0^\circ$  PFM signal. The data also likely contains background contributions due to electrostatic and other instrumental artifacts. It was thus dismissed prior to this work as an artifact of the measurement process. Despite these possible drawbacks, we note here that the qualitative features of the experimental data, namely, minimum at the center of the wall, and two peaks in amplitude on either side of the wall are clearly distinguishable and resemble the FEM theory as well as the analytical theory shown in the inset of Fig. 9. Further experiments in the future can now revisit this question with the benefit of theory and simulations presented here.

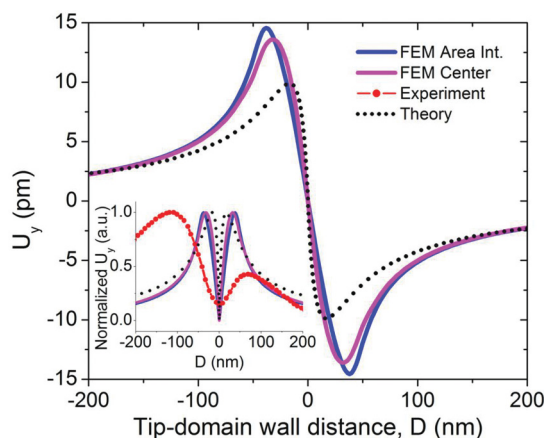


FIG. 9. (Color online) Comparison of  $90^\circ$  lateral signal from FEM results, experiment, and revised analytical theory. The legend is the same as the one in Fig. 4. Note: since the original experiment data from Ref. 13 used arbitrary unit and does not provide any phase information, only the normalized amplitude of the  $90^\circ$  lateral scan signal is shown in inset here. The FEM and revised analytical results indicate that the phase of the  $90^\circ$  lateral signal should be reversed when the tip scans across the wall.

### V. RELATIVE CONTRIBUTIONS OF THE DIFFERENT PIEZOELECTRIC COEFFICIENTS TO THE PFM SIGNALS

Since  $\text{LiNbO}_3$  belongs to point group  $3m$ , the piezoelectric matrix has four independent piezoelectric components,  $d_{15}$ ,

$d_{22}$ ,  $d_{31}$ , and  $d_{33}$ . The piezoelectric matrix is given by

$$\begin{bmatrix} 0 & 0 & 0 & 0 & d_{15} & -2d_{22} \\ -d_{22} & d_{22} & 0 & d_{15} & 0 & 0 \\ d_{31} & d_{31} & d_{33} & 0 & 0 & 0 \end{bmatrix}. \quad (2)$$

This section explores the relative contributions to these three types of PFM signals from the various components of the piezoelectric tensor. For example, it was shown in the last section that the  $d_{22}$  coefficient is critical for observing and explaining the  $90^\circ$  lateral PFM. In order to test the relative contributions of different piezoelectric coefficients, we performed the following procedure in our FEM simulations: the complete dielectric matrix and elastic tensors were kept the same as before, and the piezoelectric matrix was modified. For example, for the specific study on how  $d_{22}$  contributes to the PFM signal, only this coefficient and others related to it by symmetry considerations were retained, and the rest eliminated as follows:

$$\begin{bmatrix} 0 & 0 & 0 & 0 & 0 & -2d_{22} \\ -d_{22} & d_{22} & 0 & 0 & 0 & 0 \\ 0 & 0 & 0 & 0 & 0 & 0 \end{bmatrix}. \quad (3)$$

Table I gives detailed information on how each individual piezoelectric constant influences the PFM signal. For vertical PFM, one can clearly see that not only  $d_{33}$ , but also  $d_{15}$  contributes a comparable amplitude to the vertical displacement  $U_z$ . In other words, if we attempt to get an effective  $d_{33}$  piezoelectric constant by calculating  $d_{33}^{\text{eff}} = U_z/V$  ( $V$  is the electric voltage applied on the tip), the derived  $d_{33}^{\text{eff}}$  will be significantly larger than the true  $d_{33}$  material piezoelectric constant. This does *not* necessarily indicate any enhancement of the piezoelectric constant, which is often mistaken in the literature.<sup>52</sup> This point is particularly important in the calibration process of PFM experiments. As for the  $0^\circ$  lateral PFM, Table I indicates that  $d_{15}$  is the dominant factor leading to the torsion of the cantilever in the  $x$ - $z$  plane. This rules out all the other interpretations based on a dominant expansion/contraction mechanism in the domain-wall region (contributions from  $d_{33}$  or  $d_{31}$ ), and confirms the shearing (contribution from  $d_{15}$ ), as the main factor giving the  $x$ -direction surface displacement.<sup>39–41,53,54</sup> For the  $90^\circ$  lateral PFM, Table I indicates that  $d_{22}$  is the dominant factor resulting in the  $y$ -component displacement, leading to the torsion of the cantilever in the  $y$ - $z$  plane. It agrees with the revised analytical theory after taking  $d_{22}$  into consideration (see Appendix B).

TABLE I. The relative contributions of the  $d_{15}$ ,  $d_{22}$ ,  $d_{31}$ , and  $d_{33}$  coefficients to the three types of PFM signals, calculated from FEM (and analytical theory, shown in parentheses). Note:  $U_x$ ,  $U_y$ , and  $U_z$  are calculated when the tip lies at the position where the corresponding PFM signal get its maximum, for both FEM calculation and analytical theory. To be specific,  $U_x$  value in the table is calculated when the tip is on the domain wall (see Fig. 7);  $U_y$  value is calculated when the tip is near the domain wall (see Fig. 9);  $U_z$  is calculated when the tip is far away from the domain wall (see Fig. 4).

	$d_{15}$	$d_{22}$	$d_{31}$	$d_{33}$	Sum	Full tensor
$U_x$ , pm	55.8 (56.9)	-3.6 (0)	-2.5 (-7.5)	8.9 (14.1)	58.6 (63.5)	59.7
$U_y$ , pm	1.4 (0)	-16.8 (-10.3)	0 (0)	0 (0)	-15.4 (-10.3)	-14.5
$U_z$ , pm	-38.7 (-46.2)	1.2 (0)	2.3 (4.2)	-34.1 (-25.9)	-69.3 (-67.9)	-69.9

From Table I, the total surface displacement by simple linear summation of the contributions from each of the individual piezoelectric constants is a good approximation of the total piezoresponse from materials with full piezoelectric tensors considered. This is also reflected in the analytical theory that shows that the piezoresponse under a nonuniform electric field generated by the PFM tip may be simplified to a linear function of each piezoelectric tensor component (Eq. 5 in Ref. 37). In addition, Table I also showed the results from the revised analytical theory. Results from FEM and analytical theory match well.

## VI. DISCUSSION

In this paper we used the finite element method to explore an effective shear model in explaining the lateral PFM signal. In our simulations, the PFM process is considered *quasistatic*, which calculates the piezoelectric response with constant electric voltage applied to a static tip. This is a good approximation if the scan is performed with an ac voltage far away from the resonance frequency, and the tip scan speed is much slower than the data collection rate in the PFM experiment at each point. In addition, the domain wall in the FEM calculation is assumed to be a sharp thin wall. The results from such a sharp domain-wall assumption matched very well with the vertical PFM experiments.<sup>38</sup> We did not take into consideration any domain-wall bending, which may occur in a real experiment because the electric field immediately underneath the tip is as large as  $\sim 10^8$  V/m when a dc voltage +5 V is applied on the tip. Such domain-wall bending has been observed experimentally, where it was reported that the threshold for this domain switching at the wall is  $\sim 3$  V, which is an order of magnitude smaller than that of a single domain region far away from the wall ( $\sim 28$  V).<sup>51</sup>

In order to understand the origin of lateral PFM signal, Scrymgeour and Gopalan explored the slope model [Fig. 1(a)] in contrast to the effective shear model proposed here [Fig. 1(b)]. The slope model assumed that topographical surface slopes of the sample underneath the tip cause the PFM lateral signal.<sup>13,55</sup> However, they only took the vertical piezoresponse into consideration and attributed the topographical slope to be a result of the vertical expansion and contraction, respectively, on each side of the antiparallel domain wall, as shown in Fig. 1(a). The slope model has been criticized since then because mechanical analysis in Ref. 40 showed that the lateral contact force generated in the slope model is negligible compared with the actual

lateral force observed in experiments, which was found to be comparable to the vertical force on the tip (10 nN). Several other attempts were reported in the literature.<sup>39–41,53,54</sup> Although they all agreed that it is the surface displacement that gives rise to the lateral PFM signal, the origin of these displacements, namely, which piezoelectric tensor element dominates this lateral displacement, was identified incorrectly. References 41, 53, and 54 reported explorations of two mechanisms, lateral expansion/contraction contribution due to  $d_{31}$  and shearing contributions due to  $d_{15}$ , to explain the lateral surface displacement. However, they excluded the shear effect due to  $d_{15}$ , because they argued that the shear deformation was suppressed due to sideways clamping; they then concluded that the in-plane displacement chiefly originated from lateral expansion/contraction in the “active volume,” and attributed it to the  $d_{31}$  sign change across the domain wall. Although the “active volume” model is helpful in understanding the lateral resolution in the vertical PFM signal,<sup>54</sup> it assumes that the displacements due to the  $d_{15}$  coefficient will be clamped, and only  $d_{31}$  coefficient will have contributions to lateral PFM signal. Instead, we find that a lateral shear displacement distribution of the active volume is predominantly induced by the  $d_{15}$  coefficient, which is  $\sim 20$  times in magnitude to that from the  $d_{31}$  coefficient (see Table I). In comparison, Refs. 39 and 40 attributed the shear strain to the opposite sign change of piezoelectric constant  $d_{33}$  on the two sides of the  $180^\circ$  domain wall. Table I clearly shows that it is  $d_{15}$ , and not  $d_{31}$  or  $d_{33}$ , that dominates the in-plane  $x$ -component surface displacement of the sample and hence the  $0^\circ$  lateral PFM signal.

In addition to the vertical PFM and  $0^\circ$  lateral PFM, the  $90^\circ$  lateral PFM is also indispensable in order to get full information on the domain structure. This  $90^\circ$  lateral PFM signal is often obtained simultaneously together with the vertical PFM signal during the same scan. For the specific  $180^\circ$  domain structure of  $\text{LiNbO}_3$  studied in this paper, this signal is small compared to the other two PFM signals, which is most likely the reason for its neglect in the past. This study showed that  $d_{22}$  dominates the  $90^\circ$  lateral PFM signal obtained while scanning the  $180^\circ$   $\text{LiNbO}_3$  domain wall.

From the FEM study of the three different PFM signals, one important conclusion is that the PFM signal cannot be simply thought of as a direct reflection of either in-plane or out-of-plane components of polarization. For a  $180^\circ$  domain-wall structure, the FEM results show that not only does  $d_{33}$  contribute to the vertical PFM signal, but  $d_{15}$  also makes a comparable contribution. Furthermore, both experimental observation and numerical calculation showed that there is a comparable lateral PFM signal even without net in-plane polarization in  $\text{LiNbO}_3$ . In view of this, one can safely say that a measurable lateral PFM signal *does not imply* that there is an in-plane polarization in the sample.

The  $180^\circ$  domain wall is chosen in this study for its simplicity as well as universality, since it is present in all ferroelectrics. The FEM analysis method presented here can be applied to analyze any other domain-wall types, including  $90^\circ$  domain walls in tetragonal and orthorhombic systems, such as in  $\text{BaTiO}_3$  and  $\text{KNbO}_3$ , and  $71^\circ$  or  $109^\circ$  domain walls in rhombohedral systems such as  $\text{BiFeO}_3$ .

## VII. CONCLUSIONS

The origin of nanoscale piezoresponse across an antiparallel domain wall under a scanned bias tip has been theoretically and numerically modeled, and compared with experiments. The results from the FEM simulations quantitatively agree with the previously published experimental results. From our analysis, the effective shear model leads to lateral PFM signals observed in the experiments, thus resolved the outstanding controversy surrounding the origin of this signal. We present a detailed discussion of various piezoelectric tensor elements that contribute to the three types of PFM signals. For the  $180^\circ$  domain-twin structure in  $\text{LiNbO}_3$ , the vertical PFM signal arises mainly from piezoelectric constants  $d_{33}$  and  $d_{15}$ , the  $0^\circ$  lateral PFM signal arises mainly from  $d_{15}$ , and it was demonstrated that the  $90^\circ$  lateral PFM signal arises from  $d_{22}$ . The  $90^\circ$  lateral signal was experimentally observed before, but is theoretically predicted here. The FEM simulation method presented here is general, and may be applied to other domain structures in piezoelectric and ferroelectric materials. The understanding of lateral PFM signals presented here could be useful in the design of shear mode transducers and sensors based on periodic ferroelectric domains with  $180^\circ$  walls.<sup>56–58</sup>

## ACKNOWLEDGMENTS

This work was supported in part through National Science Foundation Grants No. DMR-0820404, No. DMR-1210588, and No. DMR-0908718. We thank the Center for Nanophase Materials Science at Oak Ridge National Laboratory for access to the scanning probe facilities. Scanning probe microscopy was performed (S.V.K.) at the Center for Nanophase Materials Sciences, which is sponsored by Oak Ridge National Laboratory by the Scientific User Facilities Division, Office of Basic Energy Sciences, US Department of Energy.

## APPENDIX A: DERIVATION OF EQ. (1) FOR AVERAGING PFM SIGNAL OVER TIP CONTACT AREA

The simplest model is to represent the contact area between the tip and the sample as an array of vertical springs with a spring constant  $k$ . For the sake of generality, in the absence of piezoelectric coupling, we assume that the (flat) punch settles to depth  $z_1$ . If we turn on coupling and if there is no punch, the surface will adopt the profile,  $z_1 + u_z(r, \phi, D)$  (see Fig. 1 for definitions). If the punch is there, it will shift and it is assumed that the total displacement of the punch is  $U_z$ .

If the adjacent spring elements do not interact with each other, the local force on each spring becomes  $k [z_1 - U_z + u_z(r, \phi, D)]$ . The total force on the punch becomes

$$F_z = \frac{1}{\pi a^2} \int_0^a \int_0^{2\pi} r k [z_1 - U_z + u_z(r, \phi, D)] dr d\phi. \quad (\text{A1})$$

Since the experiment is performed under constant load and without slipping, the force before and after the piezoelectric deformation of the sample are equal, and we have

$$\int_0^a \int_0^{2\pi} r [z_1 - U_z + u_z(r, \phi, D)] dr d\phi = \int_0^a \int_0^{2\pi} r z_1 dr d\phi \quad (\text{A2})$$

from which we derive average displacement in Eq. (1) as

$$U_z = \frac{1}{\pi a^2} \int_0^a \int_0^{2\pi} r u_z(r, \varphi, D) dr d\varphi. \quad (\text{A3})$$

A similar argument can be made for lateral displacements. Any relative motion between the tip and sample will result in a component force  $F_z$  on the vertical springs at the interface between tip and the sample. Since it is assumed that the interface is *intimate* and there is no relative slip, i.e.,  $u_{x,\text{sample}}(r, \varphi, D) = u_{x,\text{tip}}(r, \varphi, D)$ , therefore, any contribution to  $F_z$  from the relative slip will be zero. However, since the lateral position of the pivot point (Fig. 1) is fixed, the tip will twist, where the angle of twist  $\theta$  is given by  $\tan \theta = U_x/H$ , where  $U_x$  is the averaged lateral displacement, and  $H$  is the height of the cantilever tip. The lateral PFM signal is proportional to this twist.

## APPENDIX B: ANALYTICAL THEORY OF 90° LATERAL PFM SIGNAL

Perturbation approach for local piezoelectric response in PFM description was suggested by Felten *et al.*<sup>12</sup> and Scrymgeour and Gopalan.<sup>13</sup> It is based on the solution to a decoupled problem. In this case, the electric field in the material is calculated using a rigid electrostatic model (no piezoelectric coupling); the strain or stress field is calculated using constitutive relations for a piezoelectric solid, and the displacement field is evaluated using an appropriate Green's function for an isotropic or anisotropic solid. In this approximation, the PFM signal, i.e., surface displacement  $u_i(\mathbf{x}, \mathbf{y})$  at location  $\mathbf{x}$  induced by the tip at position  $\mathbf{y} = (y_1, y_2)$ , is given in Ref. 36 as

$$u_i(\mathbf{x}, \mathbf{y}) = \int_{-\infty}^{\infty} d\xi_1 \int_{-\infty}^{\infty} d\xi_2 \int_0^{\infty} d\xi_3 \frac{\partial G_{ij}(x_1 - \xi_1, x_2 - \xi_2, \xi_3)}{\partial \xi_k} \times E_l(\xi) c_{kjmn} d_{lnm}(y_1 + \xi_1, y_2 + \xi_2, \xi_3). \quad (\text{B1})$$

Here coordinate  $\mathbf{x} = (x_1, x_2, z)$  is linked to the indenter apex, coordinates  $\mathbf{y} = (y_1, y_2)$  denote the indenter position in the sample coordinate system  $\mathbf{y}$ , as shown in Fig. 1 of Ref. 36. Please note that the  $(x_1, x_2, z)$  coordinate system in Ref. 36 is left-handed, and equivalent to the  $(x, y, -z)$  direction in the coordinate system used in the current paper (see Figs. 1 and 2). Similarly, in place of using  $y_1$  in Ref. 36, we simply use  $D$  to specify the tip position in the current paper. Coefficients  $d_{lnm}$  and  $c_{kjmn}$  are position dependent components of the piezoelectric strain constant and elastic stiffness tensors, respectively.  $E_l(\mathbf{x})$  is the electric-field strength distribution produced by the probe. The Green's function for a semi-infinite medium  $G_{ij}(\mathbf{x} - \xi)$  links the eigenstrains  $c_{jlmn} d_{lnm} E_l$  to the displacement field. In the framework of the effective charge model,<sup>59,60</sup> electric-field distribution could be obtained in the form

$$E_i = V d \frac{\xi_i}{[\xi_1^2 + \xi_2^2 + (\xi_3 \gamma + d)^2]^{3/2}}, \quad i = 1, 2. \quad (\text{B2})$$

Here  $\gamma = \sqrt{\varepsilon_{33}/\varepsilon_{11}}$  is the dielectric anisotropy factor,  $d$  is the distance from the surface to the point charge  $Q$  representing the tip,  $V$  is the potential applied to the probe. For the disk-shaped electrode  $d \approx 2R_0/\pi$ , where  $R_0$  is the radius of the disk.<sup>38</sup>

It is well known that  $3m$  materials (LiNbO<sub>3</sub>, LiTaO<sub>3</sub>) in comparison with tetragonal ferroelectrics have additional components of piezoelectric tensor, namely,

$$d_{211} = -d_{222}, d_{222}, d_{112} = d_{121} = -d_{222} \quad (\text{B3})$$

(in other words it is the only one additional nontrivial component). In Voigt matrix notations,  $d_{222} \equiv d_{22}$ . Using (B3) we rewrite the core of (B1) in the form

$$\begin{aligned} & 2d_{112}c_{j112}E_1 \frac{\partial G_{ij}}{\partial \xi_1} + d_{211}c_{j111}E_2 \frac{\partial G_{ij}}{\partial \xi_1} + d_{222}c_{j122}E_2 \frac{\partial G_{ij}}{\partial \xi_1} \\ & = d_{222} \left[ -2c_{1212}E_1 \left( \frac{\partial G_{i1}}{\partial \xi_2} + \frac{\partial G_{i2}}{\partial \xi_1} \right) + E_2 (c_{1111} - c_{1122}) \left( \frac{\partial G_{i2}}{\partial \xi_2} - \frac{\partial G_{i1}}{\partial \xi_1} \right) \right] \\ & = d_{222} (c_{1111} - c_{1122}) \left[ -E_1 \left( \frac{\partial G_{i1}}{\partial \xi_2} + \frac{\partial G_{i2}}{\partial \xi_1} \right) + E_2 \left( \frac{\partial G_{i2}}{\partial \xi_2} - \frac{\partial G_{i1}}{\partial \xi_1} \right) \right]. \end{aligned} \quad (\text{B4})$$

Here we suppose the elastic isotropy of the material [hence  $2c_{1212} = (c_{1111} - c_{1122})$  and we neglected stiffness components like  $c_{1123}, c_{2223}, c_{1312}$ , which are small for LiNbO<sub>3</sub>].

The Green's function tensor for the semi-infinite isotropic elastic half plane is given by Mura<sup>61</sup> and Landau and Lifshitz:<sup>62</sup>

$$G_{ij}(x_1 - \xi_1, x_2 - \xi_2, \xi_3) = \begin{cases} \frac{1+\nu}{2\pi Y} \left[ \frac{\delta_{ij}}{R} + \frac{(x_i - \xi_i)(x_j - \xi_j)}{R^3} + \frac{1-2\nu}{R+\xi_3} \left( \delta_{ij} - \frac{(x_i - \xi_i)(x_j - \xi_j)}{R(R+\xi_3)} \right) \right] & i, j \neq 3, \\ \frac{(1+\nu)(x_i - \xi_i)}{2\pi Y} \left( \frac{-\xi_3}{R^3} - \frac{(1-2\nu)}{R(R+\xi_3)} \right) & i = 1, 2 \quad \text{and} \quad j = 3, \\ \frac{(1+\nu)(x_j - \xi_j)}{2\pi Y} \left( \frac{-\xi_3}{R^3} + \frac{(1-2\nu)}{R(R+\xi_3)} \right) & j = 1, 2 \quad \text{and} \quad i = 3, \\ \frac{1+\nu}{2\pi Y} \left( \frac{2(1-\nu)}{R} + \frac{\xi_3^2}{R^3} \right) & i = j = 3. \end{cases} \quad (\text{B5})$$

Here  $R = \sqrt{(x_1 - \xi_1)^2 + (x_2 - \xi_2)^2 + \xi_3^2}$  is radius vector,  $Y$  is Young's modulus, and  $\nu$  is the Poisson ratio. Also note that  $c_{1111} - c_{1122} = Y/(1 + \nu)$ .

All the calculations below are performed for  $\mathbf{x} = 0$  (the response directly below the tip) and infinitely thin domain walls with profile,  $d_{22} \text{sgn}(\cos \phi_0 y_1 + \sin \phi_0 y_2)$ , where the angle  $\phi_0$  gives orientations between the wall and the  $y$  axis, the wall is

perpendicular to the surface. The  $y$  axis is parallel to the one of the mirror planes of the  $3m$  system.

Using Eqs. (B1)–(B5) the contribution of  $d_{22}$  to displacement can be written as

$$u_i(0, \mathbf{y}) = d_{22} V \int_{-\infty}^{\infty} d\xi_1 \int_{-\infty}^{\infty} d\xi_2 \int_0^{\infty} d\xi_3 W_{i22}(\xi_1, \xi_2, \xi_3) \operatorname{sgn}[\cos \phi_0 (y_1 + \xi_1) + \sin \phi_0 (y_2 + \xi_2)], \quad (\text{B6})$$

where

$$W_{122}(\xi_1, \xi_2, \xi_3) = \frac{\xi_1 \xi_2 d}{2\pi [\xi_1^2 + \xi_2^2 + (\xi_3/\gamma + d)^2]^{3/2}} \left[ \frac{3(3\xi_1^2 - \xi_2^2)}{R_\xi^5} + \frac{(1-2\nu)}{R_\xi(\xi_3 + R_\xi)^2} \left( 4 - \frac{(3\xi_1^2 - \xi_2^2)(\xi_3 + 3R_\xi)}{R_\xi^2(\xi_3 + R_\xi)} \right) \right], \quad (\text{B7a})$$

$$W_{222}(\xi_1, \xi_2, \xi_3) = \frac{1}{2\pi} \frac{d}{[\xi_1^2 + \xi_2^2 + (\xi_3/\gamma + d)^2]^{3/2}} \left[ \frac{3\xi_2^2(3\xi_1^2 - \xi_2^2)}{R_\xi^5} + (1-2\nu) \left( \frac{2(\xi_1^2 - \xi_2^2)}{R_\xi(\xi_3 + R_\xi)^2} - \frac{\xi_2^2(3\xi_1^2 - \xi_2^2)(\xi_3 + 3R_\xi)}{R_\xi^3(\xi_3 + R_\xi)^3} \right) \right], \quad (\text{B7b})$$

$$W_{322}(\xi_1, \xi_2, \xi_3) = \frac{\xi_2(3\xi_1^2 - \xi_2^2)d}{2\pi(\xi_1^2 + \xi_2^2 + (\xi_3/\gamma + d)^2)^{3/2}} \left( \frac{3\xi_3}{R_\xi^5} - \frac{(1-2\nu)(\xi_3 + 2R_\xi)}{R_\xi^3(\xi_3 + R_\xi)^2} \right). \quad (\text{B7c})$$

Here  $R_\xi = \sqrt{(\xi_1)^2 + (\xi_2)^2 + \xi_3^2}$ . Below we consider  $u_2$ , which is nonzero for  $3m$ , by identically zero for domain walls in 4-mm ferroelectrics.

Taking into account the parity of  $W_{222}$ , we could rewrite (B6) and (B7b) as

$$u_2(0, \mathbf{y}) = d_{22} V_{\text{appl}} \iiint_V W_{222}(\xi_1, \xi_2, \xi_3) d\xi_1 d\xi_2 d\xi_3. \quad (\text{B8})$$

Here we introduced the range of integration  $V : \{|\xi_1 \cos \phi_0 + \xi_2 \sin \phi_0| \leq a, \xi_3 \geq 0\}$  and distance to the wall  $a \equiv y_1 \cos \phi_0 + y_2 \sin \phi_0$ . Next we introduce spherical coordinate system,  $\xi_1 = r \sin \theta \cos \varphi$ ,  $\xi_2 = r \sin \theta \sin \varphi$ ,  $\xi_3 = r \cos \theta$ , and perform integration on  $r$ :

$$u_2(0, \mathbf{y}) = d_{22} V \operatorname{sgn}(a) \frac{1}{\pi} \int_0^{\pi/2} d\theta \int_{-\pi/2+\phi_0}^{\pi/2+\phi_0} d\varphi \left( 1 - \frac{\frac{|a| \cos \theta}{\gamma} + d \sin \theta \cos(\phi - \phi_0)}{\sqrt{a^2 \sin^2 \theta + \left(\frac{|a| \cos \theta}{\gamma} + d \sin \theta \cos(\phi - \phi_0)\right)^2}} \right) w_{222}(\theta, \phi) \sin \theta, \quad (\text{B9a})$$

where

$$w_{222}(\theta, \phi) = \left[ 3(\sin \theta)^2 \frac{\cos(2\phi) - \cos(4\phi)}{2} + (1-2\nu) \left( \frac{2 \cos(2\phi)}{(\cos \theta + 1)^2} - \frac{\cos(2\phi) - \cos(4\phi)}{2} \frac{(\cos \theta + 3)(\sin \theta)^2}{(\cos \theta + 1)^3} \right) \right]. \quad (\text{B9b})$$

For the particular case  $d_{22} \operatorname{sgn}(y_1)$ , when  $\phi_0 = 0$ , the contribution of  $d_{22}$  to displacement  $u_2$ , that is nonzero for  $3m$ , is

$$u_2(0, \mathbf{y}) = d_{22} V \operatorname{sgn}(y_1) \frac{1}{\pi} \int_0^{\pi/2} d\theta \int_{-\pi/2}^{\pi/2} d\varphi \left( 1 - \frac{\frac{|y_1| \cos \theta}{\gamma} + d \sin \theta \cos(\phi)}{\sqrt{y_1^2 \sin^2 \theta + \left(\frac{|y_1| \cos \theta}{\gamma} + d \sin \theta \cos(\phi)\right)^2}} \right) w_{222}(\theta, \phi) \sin \theta. \quad (\text{B10})$$

Here  $y_1$  is the distance to the wall,

$$w_{222}(\theta, \phi) = 3(\sin \theta)^2 \frac{\cos(2\phi) - \cos(4\phi)}{2} + (1-2\nu) \left( \frac{2 \cos(2\phi)}{(\cos \theta + 1)^2} - \frac{\cos(2\phi) - \cos(4\phi)}{2} \frac{(\cos \theta + 3)(\sin \theta)^2}{(\cos \theta + 1)^3} \right). \quad (\text{B11})$$

Results of numerical integration of Eqs. (B10) and (B11) for  $\text{LiNbO}_3$  parameters are presented as a dotted curve in Fig. 9.

\* Author to whom correspondence should be addressed: dzk@psu.edu

† Author to whom correspondence should be addressed: vxg8@psu.edu

<sup>1</sup>M. Alexe, A. Gruverman, C. Harnagea, N. Zakharov, A. Pignolet, D. Hesse, and J. Scott, *Appl. Phys. Lett.* **75**, 1158 (1999).

<sup>2</sup>M. Alexe, J. Scott, C. Curran, N. Zakharov, D. Hesse, and A. Pignolet, *Appl. Phys. Lett.* **73**, 1592 (1998).

<sup>3</sup>A. Gruverman, D. Wu, and J. Scott, *Phys. Rev. Lett.* **100**, 097601 (2008).

<sup>4</sup>S. V. Kalinin, S. Jesse, B. Rodriguez, Y. Chu, R. Ramesh, E. Eliseev, and A. Morozovska, *Phys. Rev. Lett.* **100**, 155703 (2008).

<sup>5</sup>B. J. Rodriguez, S. Jesse, A. P. Baddorf, T. Zhao, Y. Chu, R. Ramesh, E. A. Eliseev, A. N. Morozovska, and S. V. Kalinin, *Nanotechnology* **18**, 405701 (2007).

- <sup>6</sup>A. Roelofs, U. Böttger, R. Waser, F. Schlaphof, S. Trogisch, and L. Eng, *Appl. Phys. Lett.* **77**, 3444 (2000).
- <sup>7</sup>V. Shvartsman, A. Y. Emelyanov, A. Kholkin, and A. Safari, *Appl. Phys. Lett.* **81**, 117 (2002).
- <sup>8</sup>A. Wu, P. Vilarinho, V. Shvartsman, G. Suchanek, and A. Kholkin, *Nanotechnology* **16**, 2587 (2005).
- <sup>9</sup>M. Alexe and A. Gruverman, *Nanoscale Characterisation of Ferroelectric Materials: Scanning Probe Microscopy Approach* (Springer, Berlin, 2004).
- <sup>10</sup>A. Gruverman and A. Kholkin, *Rep. Prog. Phys.* **69**, 2443 (2006).
- <sup>11</sup>S. Hong, *Nanoscale Phenomena in Ferroelectric Thin Films* (Kluwer Academic Publishing, Boston, MA, 2004).
- <sup>12</sup>F. Felten, G. A. Schneider, J. M. Saldana, and S. V. Kalinin, *J. Appl. Phys.* **96**, 563 (2004).
- <sup>13</sup>D. A. Scrymgeour and V. Gopalan, *Phys. Rev. B* **72**, 024103 (2005).
- <sup>14</sup>S. V. Kalinin, B. J. Rodriguez, J. D. Budai, S. Jesse, A. N. Morozovska, A. A. Bokov, and Z. G. Ye, *Phys. Rev. B* **81**, 064107 (2010).
- <sup>15</sup>V. Shvartsman and A. Kholkin, *J. Appl. Phys.* **101**, 064108 (2007).
- <sup>16</sup>V. Shvartsman, A. Kholkin, M. Tyunina, and J. Levoska, *Appl. Phys. Lett.* **86**, 222907 (2005).
- <sup>17</sup>A. Kholkin, A. Morozovska, D. Kiselev, I. Bdikin, B. Rodriguez, P. Wu, A. Bokov, Z. G. Ye, B. Dkhil, and L. Q. Chen, *Adv. Funct. Mater.* **21**, 1977 (2011).
- <sup>18</sup>M. Alexe, C. Harnagea, D. Hesse, and U. Gösele, *Appl. Phys. Lett.* **75**, 1793 (1999).
- <sup>19</sup>L. Eng, S. Grafström, C. Loppacher, F. Schlaphof, S. Trogisch, A. Roelofs, and R. Waser, *Adv. Solid State Phys.* **41**, 287 (2001).
- <sup>20</sup>A. Gruverman, O. Auciello, and H. Tokumoto, *J. Vac. Sci. Technol. B* **14**, 602 (1996).
- <sup>21</sup>H. Guo, J. Xu, I. Wilson, Z. Xie, E. Luo, S. Hong, and H. Yan, *Appl. Phys. Lett.* **81**, 715 (2002).
- <sup>22</sup>C. Harnagea, *Local Piezoelectric Response and Domain Structures in Ferroelectric Thin Films Investigated by Voltage-Modulated Force Microscopy* (Universitäts-und Landesbibliothek, Halle (Saale), 2001).
- <sup>23</sup>S. Kalinin, B. Rodriguez, S. Jesse, Y. Chu, T. Zhao, R. Ramesh, S. Choudhury, L. Chen, E. Eliseev, and A. Morozovska, *Proc. Natl. Acad. Sci. USA* **104**, 20204 (2007).
- <sup>24</sup>V. Shvartsman, N. Pertsev, J. Herrero, C. Zaldo, and A. Kholkin, *J. Appl. Phys.* **97**, 104105 (2005).
- <sup>25</sup>D. Xue, S. Wu, Y. Zhu, K. Terabe, K. Kitamura, and J. Wang, *Chem. Phys. Lett.* **377**, 475 (2003).
- <sup>26</sup>S. Jesse, H. N. Lee, and S. V. Kalinin, *Rev. Sci. Instrum.* **77**, 073702 (2006).
- <sup>27</sup>B. J. Rodriguez, S. Jesse, A. P. Baddorf, T. Zhao, Y. H. Chu, R. Ramesh, E. A. Eliseev, A. N. Morozovska, and S. V. Kalinin, *Nanotechnology* **18**, 5701 (2007).
- <sup>28</sup>S. V. Kalinin, A. N. Morozovska, L. Q. Chen, and B. J. Rodriguez, *Rep. Prog. Phys.* **73**, 056502 (2010).
- <sup>29</sup>A. Gruverman and A. Kholkin, *Rep. Prog. Phys.* **69**, 2443 (2006).
- <sup>30</sup>N. Balke, I. Bdikin, S. V. Kalinin, and A. L. Kholkin, *J. Am. Ceram. Soc.* **92**, 1629 (2009).
- <sup>31</sup>S. Baek, H. Jang, C. Folkman, Y. Li, B. Winchester, J. Zhang, Q. He, Y. Chu, C. Nelson, and M. Rzechowski, *Nat. Mater.* **9**, 309 (2010).
- <sup>32</sup>B. J. Rodriguez, S. Choudhury, Y. Chu, A. Bhattacharyya, S. Jesse, K. Seal, A. P. Baddorf, R. Ramesh, L. Q. Chen, and S. V. Kalinin, *Adv. Funct. Mater.* **19**, 2053 (2009).
- <sup>33</sup>N. Balke, S. Choudhury, S. Jesse, M. Huijben, Y. Chu, A. Baddorf, L. Chen, R. Ramesh, and S. Kalinin, *Nat. Nanotechnol.* **4**, 868 (2009).
- <sup>34</sup>E. A. Eliseev, S. V. Kalinin, S. Jesse, S. L. Bravina, and A. N. Morozovska, *J. Appl. Phys.* **102**, 014109 (2007).
- <sup>35</sup>S. V. Kalinin, E. A. Eliseev, and A. N. Morozovska, *Appl. Phys. Lett.* **88**, 232904 (2006).
- <sup>36</sup>A. N. Morozovska, E. A. Eliseev, S. L. Bravina, and S. V. Kalinin, *Phys. Rev. B* **75**, 174109 (2007).
- <sup>37</sup>A. N. Morozovska, E. A. Eliseev, G. S. Svechnikov, V. Gopalan, and S. V. Kalinin, *J. Appl. Phys.* **103**, 124110 (2008).
- <sup>38</sup>L. Tian, A. Vasudevarao, A. N. Morozovska, E. A. Eliseev, S. V. Kalinin, and V. Gopalan, *J. Appl. Phys.* **104**, 074110 (2008).
- <sup>39</sup>J. Guyonnet, H. Bea, F. Guy, S. Gariglio, S. Fusil, K. Bouzehouane, J. M. Triscone, and P. Paruch, *Appl. Phys. Lett.* **95**, 132902 (2009).
- <sup>40</sup>J. Guyonnet, H. Bea, and P. Paruch, *J. Appl. Phys.* **108**, 042002 (2010).
- <sup>41</sup>F. Johann, T. Jungk, M. Lilienblum, Á. Hoffmann, and E. Soergel, *Appl. Phys. Lett.* **97**, 102902 (2010).
- <sup>42</sup>T. Jungk, Á. Hoffmann, and E. Soergel, *Appl. Phys. Lett.* **89**, 042901 (2006).
- <sup>43</sup>S. V. Kalinin, B. J. Rodriguez, S. Jesse, E. Karapetian, B. Mirman, E. A. Eliseev, and A. N. Morozovska, in *Annual Review of Materials Research* (Annual Reviews, Palo Alto, 2007), Vol. 37, pp. 189–238.
- <sup>44</sup>T. Choi, S. Lee, Y. Choi, V. Kiryukhin, and S. W. Cheong, *Science* **324**, 63 (2009).
- <sup>45</sup>T. Zhao, A. Scholl, F. Zavaliche, K. Lee, M. Barry, A. Doran, M. Cruz, Y. Chu, C. Ederer, and N. Spaldin, *Nat. Mater.* **5**, 823 (2006).
- <sup>46</sup>B. Rodriguez, X. Gao, L. Liu, W. Lee, I. Naumov, A. Bratkovsky, D. Hesse, and M. Alexe, *Nano Lett.* **9**, 1127 (2009).
- <sup>47</sup>M. Jazbinsek and M. Zgonik, *Appl. Phys. B* **74**, 407 (2002).
- <sup>48</sup>L. Tian, Ph.D. thesis, Pennsylvania State University, State College, 2006.
- <sup>49</sup>S. V. Kalinin, A. Rar, and S. Jesse, *IEEE Trans. Ultrason. Ferroelectr. Freq. Control* **53**, 2226 (2006).
- <sup>50</sup>S. V. Kalinin, B. J. Rodriguez, S. Jesse, J. Shin, A. P. Baddorf, P. Gupta, H. Jain, D. B. Williams, and A. Gruverman, *Microsc. Microanal.* **12**, 206 (2006).
- <sup>51</sup>V. R. Aravind, A. N. Morozovska, S. Bhattacharyya, D. Lee, S. Jesse, I. Grinberg, Y. L. Li, S. Choudhury, P. Wu, K. Seal, A. M. Rappe, S. V. Svechnikov, E. A. Eliseev, S. R. Phillpot, L. Q. Chen, V. Gopalan, and S. V. Kalinin, *Phys. Rev. B* **82**, 024111 (2010).
- <sup>52</sup>M. H. Zhao, Z. L. Wang, and S. X. Mao, *Nano Lett.* **4**, 587 (2004).
- <sup>53</sup>T. Jungk, A. Hoffmann, and E. Soergel, *New J. Phys.* **11**, 033029 (2009).

- <sup>54</sup>E. Soergel, *J. Phys. D: Appl. Phys.* **44**, 464003 (2011).
- <sup>55</sup>J. Wittborn, C. Canalias, K. V. Rao, R. Clemens, H. Karlsson, and F. Laurell, *Appl. Phys. Lett.* **80**, 1622 (2002).
- <sup>56</sup>A. K. S. Kumar, P. Paruch, J. M. Triscone, W. Daniau, S. Ballandras, L. Pellegrino, D. Marré, and T. Tybell, *Appl. Phys. Lett.* **85**, 1757 (2004).
- <sup>57</sup>E. Courjon, J. Masson, D. Gachon, L. Gauthier-Manuel, W. Daniau, N. Bodin, S. Ballandras, and J. Hauden, in *Frequency Control Symposium, 2007 Joint with the 21st European Frequency and Time Forum. IEEE International* (IEEE, New York, 2007), pp. 1073–1076.
- <sup>58</sup>E. Courjon, N. Courjal, W. Daniau, G. Lengaigne, L. Gauthier-Manuel, S. Ballandras, and J. Hauden, *J. Appl. Phys.* **102**, 114107 (2007).
- <sup>59</sup>A. N. Morozovska, E. A. Eliseev, and S. V. Kalinin, *J. Appl. Phys.* **102**, 074105 (2007).
- <sup>60</sup>A. N. Morozovska, S. V. Svechnikov, E. A. Eliseev, and S. V. Kalinin, *Phys. Rev. B* **76**, 054123 (2007).
- <sup>61</sup>T. Mura, *Micromechanics of Defects in Solids* (Kluwer, Dordrecht, 1987).
- <sup>62</sup>L. Landau and E. Lifshitz (Butterworth-Heinemann, Oxford, UK, 1998).